Antarctic sub-shelf melt rates via PICO

Ronja Reese[1,2], Torsten Albrecht[1], Matthias Mengel[1], Xylar Asay-Davis[1], and Ricarda Winkelmann[1,2]

[1] Potsdam Institute for Climate Impact Research (PIK), Member of the Leibniz Association, P.O. Box 60 12 03, D-14412 Potsdam, Germany

[2] University of Potsdam, Institute of Physics and Astronomy, Karl-Liebknecht-Str. 24-25, 14476 Potsdam, Germany

Correspondence to: Ricarda Winkelmann (ricarda.winkelmann@pik-potsdam.de)

Abstract. Ocean-induced melting below ice shelves is one of the dominant drivers for mass loss from the Antarctic Ice Sheet at present. An appropriate representation of sub-shelf melt rates is therefore essential for model simulations of marine-based ice sheet evolution. Continental-scale ice sheet models often rely on simple melt-parameterizations, in particular for long-term simulations, when fully coupled ice-ocean interaction becomes computationally too expensive. Such parameterizations can

5   account for the influence of the local depth of the ice-shelf draft or its slope on melting. However, they do not capture the effect of ocean circulation underneath the ice-shelf. Here we present the Potsdam Ice-shelf Cavity mOdel (PICO), which simulates the vertical overturning circulation in ice-shelf cavities and thus enables the computation of sub-shelf melt rates consistent with this circulation. PICO is based on an ocean box model that coarsely resolves ice shelf cavities and uses a boundary layer melt formulation. We implement it as a module of the Parallel Ice Sheet Model (PISM) and evaluate its performance under

10 present-day conditions of the Southern Ocean. The two-dimensional melt rate fields provided by the model reproduce the typical pattern of comparably high melting near the grounding line and lower melting or refreezing towards the calving front. PICO captures the wide range of melt rates observed for Antarctic ice shelves, with an average of about $0.1\,\mathrm{m\,a^{-1}}$ for cold sub-shelf cavities, for example underneath Ross or Ronne ice shelves, to $12\,\mathrm{m\,a^{-1}}$ for warm cavities such as in the Amundsen Sea region. This makes PICO a computationally-feasible and more physical alternative to melt parameterizations purely based

15 on ice draft geometry.

1   Introduction

Dynamic ice discharge across the grounding lines into floating ice shelves is the main mass loss process of the Antarctic Ice Sheet. Surrounding most of Antarctica's coastlines, the ice shelves themselves lose mass by ocean-induced melting from below or calving of icebergs (Depoorter et al., 2013; Liu et al., 2015). Observations show that many Antarctic ice shelves are thinning

20 at present, driven by enhanced sub-shelf melting (Pritchard et al., 2012; Paolo et al., 2015). Thinning reduces the ice shelves' buttressing potential, *i.e.*, the restraining force at the grounding line provided by the ice shelves (Thomas, 1979; Dupont and Alley, 2005; Gudmundsson et al., 2012), and can thereby accelerate upstream glacier flow. The observed acceleration of tributary glaciers is seen as the major contributor to the current mass loss in the West Antarctic Ice Sheet (Pritchard et al., 2012). In particular, the recent dynamic ice loss in the Amundsen Sea sector (MacGregor et al., 2012; Mouginot et al., 2014)

25 is associated with high melt rates that result from inflow of relatively warm circumpolar deep water (CDW) in the ice shelf

cavities (Holland et al., 2008a; Jacobs et al., 2011; Pritchard et al., 2012; Schmidtko et al., 2014; Hellmer et al., 2017). Also in East Antarctica, particularly at Totten glacier, as well as along the Southern Antarctic Peninsula, glacier thinning seems to be linked to CDW reaching the deep grounding lines (Greenbaum et al., 2015; Wouters et al., 2015). An appropriate representation of melt rates at the ice-ocean interface is hence crucial for simulating the dynamics of the Antarctic Ice Sheet. Melting in ice-

5   shelf cavities can occur in different modes that depend on the ocean properties in the proximity of the ice shelf, the topography of the ocean bed and the ice-shelf subsurface (Jacobs et al., 1992). Antarctica's ice shelf cavities can be classified into "cold" and "warm" with typical mean melt rates ranging from $\mathcal{O}(0.1 - 1.0)\,\mathrm{m\,a^{-1}}$ in "cold" cavities as for the Filchner-Ronne Ice Shelf and $\mathcal{O}(10)\,\mathrm{m\,a^{-1}}$ in "warm" cavities like the one adjacent to Pine Island Glacier (Joughin et al., 2012). For the "cold" cavities of the large Ross, Filchner-Ronne and Amery ice shelves, freezing to the shelf base is observed in the shallower areas

10 near the center of the ice shelf and towards the calving front (Rignot et al., 2013; Moholdt et al., 2014).

Since the stability of the ice sheet is strongly linked to the dynamics of the buttressing ice shelves, it is essential to adequately represent their mass balance. A number of parameterizations with different levels of complexity have been developed to capture the effect of sub-shelf melting. Simplistic parameterizations that depend on the local ocean and ice-shelf properties have been applied in long-term and large-scale ice sheet simulations (Joughin et al., 2014; Martin et al., 2011; Pollard and DeConto,

15 2012; Favier et al., 2014). These parameterizations make melt rates piece-wise linear functions of the depth of the ice-shelf draft (Beckmann and Goosse, 2003) or of the slope of the ice-shelf base (Little et al., 2012). Other models describe the evolution of melt-water plumes forming at the ice-shelf base (Jenkins, 1991). Plumes evolve depending on the ice-shelf draft and slope, sub-glacial discharge and entrainment of ambient ocean water. This approach has been applied to models with characteristic conditions for Antarctic ice shelves (Holland et al., 2007; Payne et al., 2007) and for Greenland outlet glaciers and fjord

20 systems (Jenkins, 2011; Carroll et al., 2015). Interactively coupled ice-ocean models that resolve both the ice flow and the water circulation below ice shelves are now becoming available (Goldberg et al., 2012; Thoma et al., 2015; Seroussi et al., 2017; De Rydt and Gudmundsson, 2016). There is a community effort to better understand effects of ice-ocean interaction in such coupled models (Asay-Davis et al., 2016). However, as ocean models have many more degrees of freedom than ice sheet models and require for much shorter time steps, coupled simulations are currently limited to short time scales (on the order of

25 decades to centuries).

Here, we present the Potsdam Ice-shelf Cavity mOdel (PICO), which provides sub-shelf melt rates in a computationally efficient manner and resolves the basic vertical overturning circulation in ice shelf cavities driven by the ice pump (Lewis and Perkin, 1986). It is based on the earlier work of Olbers and Hellmer (2010) and is implemented as a module in the Parallel Ice Sheet Model (PISM: Bueler and Brown, 2009; Winkelmann et al., 2011)[1]. Ocean temperature and salinity at the depth of

30 the bathymetry in the continental shelf region serve as input data. PICO allows for long-term simulations (on centennial to millennial time scales) and for large ensembles of simulations which makes it applicable, for example, in paleo-climate studies or as a coupling module between ice-sheet and Earth System models.

In this paper, we give a brief overview of the cavity circulation and melt physics and describe the ocean box geometry in PICO and implementation in PISM in Sect. 2. In Section 3, we derive a valid parameter range for present-day Antarctica

---

[1]http:\\www.pism_docs.org

Table 1. PICO parameters and typical values.

Parameter	Symbol	Value	Unit
Salinity coefficient of freezing equation	a	-0.0572	$^\circ\mathrm{C\,PSU}^{-1}$
Constant coefficient of freezing equation	b	0.0788	$^\circ\mathrm{C}$
Pressure coefficient of freezing equation	c	7.77×10^{-8}	$^\circ\mathrm{C\,Pa}^{-1}$
Thermal expansion coefficient in EOS	α	7.5×10^{-5}	$^\circ\mathrm{C}^{-1}$
Salt contraction coefficient in EOS	β	7.7×10^{-4}	PSU^{-1}
Reference density in EOS	ρ_*	1033	$\mathrm{kg\,m}^{-3}$
Latent heat of fusion	L	3.34×10^5	$\mathrm{J\,kg}^{-1}$
Heat capacity of sea water	c_p	$3,974$	$\mathrm{J\,kg}^{-1}\,^\circ\mathrm{C}^{-1}$
Density of ice	ρ_i	910	$\mathrm{kg\,m}^{-3}$
Density of sea water	ρ_w	1028	$\mathrm{kg\,m}^{-3}$
Turbulent salinity exchange velocity	γ_S	2×10^{-6}	$\mathrm{m\,s}^{-1}$
Turbulent temperature exchange velocity	γ_T	5×10^{-5}	$\mathrm{m\,s}^{-1}$
Effective turbulent temperature exchange velocity	γ_T^*	2×10^{-5}	$\mathrm{m\,s}^{-1}$
Overturning strength	C	1×10^6	$\mathrm{m}^3\,\mathrm{s}^{-1}$

The coefficients in the equation of state (EOS), the turbulent exchange velocities for heat and salt are taken from Olbers and Hellmer (2010). We linearized the potential freezing temperature equation with a least-squares fit with salinity values over a range of 20-40 PSU and pressure values of 0-10^7 Pa using Gibbs SeaWater Oceanographic Package of TEOS-10 (McDougall and Barker, 2011). All values are kept constant, except for γ_T^* and C, which vary between experiments. The values of these two parameters are the best fit values analysed in Sect. 3.1.

and compare the resulting sub-shelf melt rates to observational data. This is followed by a discussion of the applicability and limitations of the model (Sect. 4) and conclusions (Sect. 5).

2 Model description

PICO is developed from the ocean box model of Olbers and Hellmer (2010), henceforth OH10. The OH10 model is designed
5 to capture the basic overturning circulation in ice shelf cavities which is driven by the "ice pump" mechanism: melting at the ice shelf base near the grounding line reduces salinity and the ambient ocean water becomes buoyant, rising along the ice shelf base towards the calving front. Since the ocean temperatures on the Antarctic continental shelf are generally close to the local freezing point, density variations are primarily controlled by salinity changes. Melting at the ice-shelf base hence reduces the density of ambient water masses, resulting in a haline-driven circulation. Buoyant water rising along the shelf base draws in
10 ocean water at depth, which flows across the continental shelf towards the deep grounding lines of the ice shelves. The warmer these water masses are, the stronger is the melting-induced ice pump. The OH10 box model describes the relevant physical processes and captures this vertical overturning circulation by defining consecutive boxes following the flow within the ice shelf cavity.
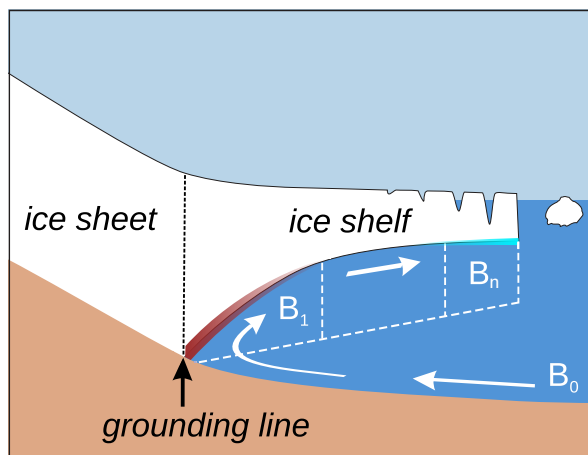
Figure 1. Schematic view of the PICO model. The model mimics the overturning circulation in ice shelf cavities: Ocean water from box B_0 enters the ice shelf cavity at the depth of the sea floor and is advected to the grounding line box B_1. Freshwater influx from melting at the ice shelf base makes the water buoyant, causing it to rise. The cavity is divided into n boxes along the ice shelf base. Generally, the highest melt rates can be found near the grounding line, with lower melt rates or refreezing towards the calving front.

The strength of the overturning flux q is determined from the density difference between the incoming water masses on the continental shelf and the buoyant water masses near the deep grounding lines of the ice shelf. As PICO is implemented in an ice sheet model with characteristic time scales much slower than typical response times of the ocean, we assume steady-state ocean conditions and hence reduce the complexity of the governing equations of the OH10 model. We assume stable vertical strati-

5   fication, which motivates neglecting the diffusive heat and salt transport between boxes[2]. Without diffusive transport between the boxes, some of the original ocean boxes from OH10 become passive and can be incorporated into the governing equations of the set of boxes used in PICO. We explicitly model a single open ocean box which provides the boundary conditions for the boxes adjacent to the ice shelf base following the overturning circulation, as shown in Fig. 1. In order to better resolve the complex melt patterns, PICO adapts the number of boxes based on the evolving geometry of the ice shelf. These simplifying

10   assumptions allow us to analytically solve the system of governing equations, which is presented in the following two sections. A detailed derivation of the analytic solutions is given in Appendix A. In Sect. 2.3, we describe how the ice-model grid relates to the ocean box geometry of PICO. The system of equations is solved locally on the ice-model grid, as described in Sect. 2.4. Table 1 summarizes the model parameters and typical values.

---

[2]OH10 discuss a circulation state for an unstable vertical water column, which would imply a high (parametrized) diffusive transport between boxes. They find that this state only occurs transiently (Olbers and Hellmer, 2010, Sect. 2).

2.1 Physics of the overturning circulation in ice shelf cavities

PICO solves for the transport of heat and salt between the ocean boxes as depicted in Fig. 1. Although box B_0, which is located at depth between the ice shelf front and the edge of the continental shelf, does not extend into the shelf cavity, its properties are transported unchanged from box B_0 to box B_1 near the grounding line. The heat and salt balances for all boxes in contact

5 with the ice shelf base (boxes B_k for $k \in \{1, \ldots n\}$) can be written as

$$V_k \dot{T}_k = q T_{k-1} - q T_k + A_k m_k T_{bk} - A_k m_k T_k + A_k \gamma_T (T_{bk} - T_k) \tag{1}$$

$$V_k \dot{S}_k = q S_{k-1} - q S_k + A_k m_k S_{bk} - A_k m_k S_k + A_k \gamma_S (S_{bk} - S_k). \tag{2}$$

The local application of these equations for each ice model cell is described in Sect. 2.4. Since we assume steady circulation, the terms on the left-hand side are neglected. For the box B_k with volume V_k, heat or salt content change due to advection

10 from the adjacent box B_{k-1} with overturning flux q (first term on the right-hand side) and due to advection to the neighboring box B_{k+1} (or the open ocean for $k = n$) with overturning flux q (second term). Vertical melt flux into the box B_k across the ice-ocean interface with area A_k (third term) and out of the box (fourth term) play a minor role and are neglected in the analytic solution of the equation system employed in PICO (a detailed discussion of these terms is given in Jenkins et al., 2001). The melt rate m_k is negative if ambient water freezes to the shelf base. The last term represents heat and salt changes via turbulent,

15 vertical diffusion across the boundary layer beneath the ice-ocean interface. The parameters γ_T and γ_S are the turbulent heat and salt exchange velocities which we assume to be constant.

The overturning flux $q > 0$ is assumed to be driven by the density difference between the ocean reservoir box B_0 and the grounding line box B_1. This is parametrized as

$$q = C(\rho_0 - \rho_1) \tag{3}$$

20 where C is a constant overturning coefficient that captures effects of friction, rotation and bottom formstress[3]. The circulation strength in PICO is hence determined by density changes through sub-shelf melting in the grounding zone box B_1. From there, water follows the ice shelf base towards the open ocean assuming the overturning flux q to be the same for all subsequent boxes. Ocean water densities are computed assuming a linear approximation of the equation of state

$$\rho = \rho_*(-\alpha T + \beta S) \tag{4}$$

25 where α, β and ρ_* are constants with values given in Table 1.

2.2 Melting physics

Melting physics are derived from the widely used 3-equation model (Hellmer and Olbers, 1989; Holland and Jenkins, 1999) which assumes the presence of a boundary layer below the ice-ocean interface. The temperature at this interface in box B_k is assumed to be at the in-situ freezing point T_{bk}, which is linearly approximated by

30 $$T_{bk} = a S_{bk} + b - c p_k, \tag{5}$$

---

[3]For a more detailed discussion see Olbers and Hellmer (2010, Sect. 2).

where p_k is the overburden pressure, here calculated as static-fluid pressure given by the weight of the ice on top. At the ice-ocean interface, the heat flux from the ambient ocean across the boundary layer due to turbulent mixing, $Q_T = \rho_w c_p \gamma_T (T_{bk} - T_k)$, equals the heat flux due to melting or freezing $Q_{Tb} = -\rho_i L m_k$. We here neglect heat flux into the ice, the heat balance equation thus reads

$$\gamma_T (T_{bk} - T_k) = -\nu \lambda m_k \tag{6}$$

where $\nu = \rho_i / \rho_w \sim 0.89$, $\lambda = L/c_p \sim 84\,^\circ\mathrm{C}$. We obtain the salt flux boundary condition as the balance between turbulent salt transfer across the boundary layer, $Q_S = \rho_w \gamma_S (S_{bk} - S_k)$, and reduced salinity due to melt water input, $Q_{Sb} = -\rho_i S_{bk} m_k$,

$$\gamma_S (S_{bk} - S_k) = -\nu S_{bk} m_k. \tag{7}$$

To compute melt rates, we apply a simplified version of the 3-equations model (McPhee, 1992, 1999; Holland and Jenkins, 1999) which allows for a simple, analytic solution of the system of governing equations. It has been shown that this formulation yields realistic heat fluxes (McPhee, 1992, 1999). This simplification is used only for melt rates, the 3-equations formulation is applied from then on, with details laid out in Appendix A. Melt rates are given by

$$m_k = -\frac{\gamma_T^*}{\nu \lambda} (a S_k + b - c p_k - T_k) \tag{8}$$

with ambient ocean temperature T_k and salinity S_k in box B_k. Here, we use the effective turbulent heat exchange coefficient γ_T^*. The relation between γ_T and γ_T^* is discussed in the Appendix A.

2.3 PICO ocean box geometry

PICO is implemented as a module in the three-dimensional ice sheet model PISM as described in Sect. 2.4. Since the original system of box-model equations is formulated for only one horizontal and one vertical dimension, it needed to be extended for the use in the three-dimensional ice sheet model. To this aim, PICO distinguishes *basins*, which are chosen to encompass large ice shelf embayments and areas of similar ocean conditions. The standard basins used for Antarctica are shown in Fig. 2, see Sect. 3. The system of governing equations as described in the previous two sections are solved for each basin independently.

For any basin D, we determine the number of ocean boxes n_D based on the size and geometry of the ice shelves such that larger ice shelves are resolved with more boxes. The number of boxes is defined separately for each basin by interpolating between 1 and $n_{\max}$ depending on the geometry of the ice shelves within that basin. The maximum number of boxes $n_{\max}$ is a model parameter; a value of 5 is used for the Antarctic setup, as discussed further in Sect 3.2. We determine the number of boxes n_D for the basin D with

$$n_D = 1 + \mathrm{rd}\left(\sqrt{d_{\mathrm{GL}}(D)/d_{\max}}\,(n_{\max} - 1)\right) \tag{9}$$

where rd rounds to the nearest integer. Here, $d_{\mathrm{GL}}(x,y)$ is the local distance to the grounding line from an ice-model grid cell with horizontal coordinates (x,y), $d_{\mathrm{GL}}(D)$ the maximum distance within basin D and $d_{\max}$ the maximum distance to the grounding line in the entire domain. PICO adapts the ocean boxes to the evolving ice shelves at every time step.

Knowing the maximum number of boxes n_D for a basin D, we next define the ocean boxes underneath the ice shelves within that basin. The extent of boxes $B_1, \ldots, B_{n_D}$ is determined using the distance to the grounding line and the shelf front. The non-dimensional *relative distance to the grounding line* r is defined as

$$r(x,y) = d_{\mathrm{GL}}(x,y)/(d_{\mathrm{GL}}(x,y) + d_{\mathrm{IF}}(x,y)) \tag{10}$$

with $d_{\mathrm{IF}}(x,y)$ the horizontal distance to the ice front. We assign all ice cells with horizontal coordinates $(x,y) \in D$ to box B_k if the following condition is met

$$1 - \sqrt{(n_D - k + 1)/n_D} \le r(x,y) \le 1 - \sqrt{(n_D - k)/n_D}. \tag{11}$$

This leads to comparable areas for the different boxes within a basin, which is motivated in Appendix B. Thus, for example, the box B_1 adjacent to the grounding line interacts with all ice shelf grid cells with $0 \le r \le 1 - \sqrt{(n_D - 1)/n_D}$. Figure 3 shows an example of the ocean box areas for Antarctica.

2.4 Implementation in the Parallel Ice Sheet Model

PICO is implemented in the open-source Parallel Ice Sheet Model (PISM: Bueler and Brown, 2009; Winkelmann et al., 2011). In the 3d, thermo-mechanically coupled, finite-difference model, ice velocities are computed through a superposition of the shallow approximations for the slow, shear-dominated flow in ice sheets (Hutter, 1983, SIA) and the fast, membrane-like flow in ice streams and ice shelves (Morland, 1987, SSA). In PISM, the grounding lines (diagnosed via the flotation criterion) and ice fronts evolve freely. Grounding line movement has been evaluated in the model intercomparison project MISMIP3d (Pattyn et al., 2013; Feldmann et al., 2014).

Time-stepping in PICO is the same as in the ice-sheet model. The cavity model provides sub-shelf melt rates and temperatures at the ice-ocean boundary to PISM, with temperatures being at the in-situ freezing point. PISM supplies the evolving ice-shelf geometry to PICO, which in turn updates in each time step the ocean box geometry to the ice-shelf geometry as described in Sect. 2.3.

PICO computes the melt rates progressively over the ocean boxes, independently for each basin. Since the ice-sheet model has a much higher resolution, each ocean box interacts with a number of ice shelf grid cells. PICO applies the analytic solutions of the system of governing equations summarized in Sect. 2.1 and 2.2 locally to the ice model grid as detailed below. Model parameters that are varied between the experiments are the effective turbulent heat exchange velocity γ_T^* from the melt parametrization described in Sect. 2.2 and the overturning coefficient C described in Sect. 2.1. Despite the distinction into basins, the same parameter values are applied for the entire ice-sheet.

Input for PICO in the ocean reservoir box B_0 is data from observations or large-scale ocean models in front of the ice shelves. Temperature T_0 and salinity S_0 are averaged at the depth of the bathymetry in the continental shelf region. In box B_1 adjacent to the grounding line, PICO solves the system of governing equations in each ice grid cell (x,y) to attain the overturning flux $q(x,y)$, temperature $T_1(x,y)$, salinity $S_1(x,y)$ and the melting $m_1(x,y)$ at its ice-ocean interface (given by the local solution of Eq. 3, Eq. A12, Eq. A8 and Eq. 8, respectively). The model proceeds progressively from box B_k to box

B_{k+1} to solve for sub-shelf melt rate $m_{k+1}(x,y)$, ambient ocean temperature $T_{k+1}(x,y)$ and salinity $S_{k+1}(x,y)$ (given by the local solution of Eqn. 13, Eqn. A13 and Eqn. A8, respectively) based on the previous solutions S_k and T_k in box B_k and conditions at the ice-ocean interface. PICO provides the boundary conditions T_k and S_k to box B_{k+1} as the average over the ice-grid cells along the boundary between boxes B_k and B_{k+1} ensuring a smooth transition of sub-shelf melt rates and ocean water properties, *i.e.*,

$$T_k = \langle T_k(x,y) \text{ with } (x,y) \text{ in } B_k \text{ and adjacent to } B_{k+1} \rangle \tag{12}$$

and analogously for S_k, where $\langle \, \rangle$ denotes the average.

The overturning is solved in Box B_1 and given by $q = \langle q(x,y) \text{ with } (x,y) \text{ in } B_1 \text{ and adjacent to } B_2 \rangle$. Melt rates in box B_k are computed using the local overburden pressure $p_k(x,y)$ in each ice shelf grid cell that is given by the weight of the ice column provided by PISM, *i.e.*,

$$m_k(x,y) = -\frac{\gamma_T^*}{\nu\lambda}(aS_k(x,y) + b - cp_k(x,y) - T_k(x,y)). \tag{13}$$

This reflects the pressure dependence of heat available for melting and leads to a depth-dependent melt rate pattern within each box. The implications for energy and mass conservation are discussed in Sect. 3.2 and Sect. 4.

3 Results for present-day Antarctica

We apply PICO to compute sub-shelf melt rates for all Antarctic ice shelves under present-day conditions. Based on Zwally et al. (2012), we determine 19 basins of the Antarctic Ice Sheet and extend these to the attached ice shelves and the surrounding Southern Ocean (Fig. 2). We combine drainage sectors feeding the same ice shelf, *e.g.*, all contributory inlets to Filchner-Ronne or Ross Ice Shelves. We also consolidate the basins 'IceSat21' and 'IceSat22' (Pine Island Glacier and Thwaites Glacier) as well as 'IceSat7' and 'IceSat8' in East Antarctica. Ocean conditions in box B_0 are given by observations of temperature (converted to potential temperature) and salinity (converted to practical salinity) of the water masses occupying the sea floor on the continental shelf (Schmidtko et al., 2014), averaged over the time period 1975 to 2012. Figure 2 shows the basin-mean ocean temperature (shadings and numbers) and salinity (numbers) used as input values. Here, we use $n_{\max} = 5$ from which PICO determines the number of ocean boxes in each basin via Eq. 9. Figure 3 displays the resulting extent of the ocean boxes for Antarctica, ordered in elongated bands beneath the ice shelves. For the large ice-shelf cavities of Filchner-Ronne and Ross the ice-ocean boundary is divided into five ocean boxes while smaller ice shelves have two to four boxes (see Table 2). Introducing more than five ocean boxes has a negligible effect on the melt rates, as discussed in Sect. 3.2.

To validate our model, we run diagnostic simulations with PISM+PICO based on bed topography and ice thickness from BEDMAP2 (Fretwell et al., 2013) mapped to a grid with $5\,\mathrm{km}$ horizontal resolution. Diagnostic simulations allow us to asses the sensitivity of the model to the parameters C and γ_T^* and to the number of boxes $n_{\max}$ as well as the ice model resolution.

The Cryosphere

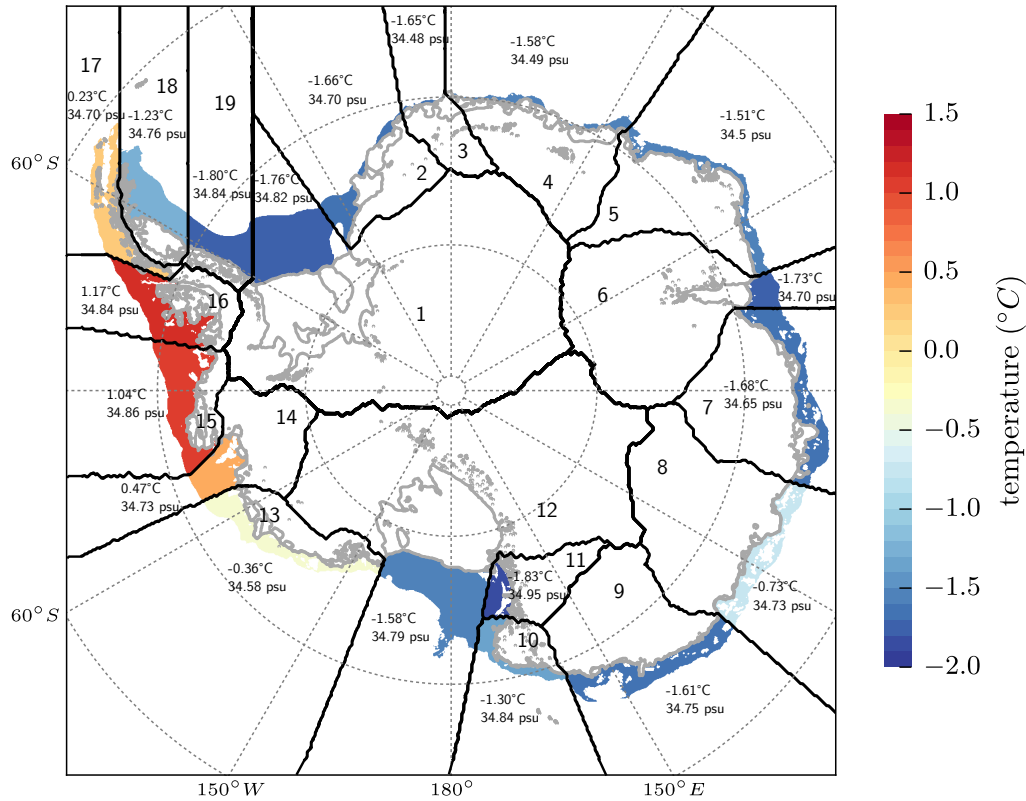Discussions

Open Access

EGU

Figure 2. PICO input for Antarctic basins. The ice sheet, ice shelves and the surrounding Southern Ocean are split into 19 basins that are based on Zwally et al. (2012) and indicated by black contour lines and labels. For each basin, the governing equations are solved separately with the respective oceanic boundary conditions. Numbers show the temperature and salinity input in box B_0, obtained by averaging observed properties of the ocean water in front of the ice shelf cavities at depth of the continental shelf (Schmidtko et al., 2014), indicated by the color shading. Grey lines show Antarctic grounding lines and ice shelf fronts (Fretwell et al., 2013).

3.1 Sensitivity to model parameters C and γ_T^*

We test the sensitivity of sub-shelf melt rates to the model parameters for overturning strength $C \in [0.1, 9]\,\mathrm{Sv}$ and the effective turbulent heat exchange velocity $\gamma_T^* \in [5 \times 10^{-6}, 1 \times 10^{-4}]\,\mathrm{m\,s^{-1}}$. These ranges encompass the values identified in OH10, discussed further in Appendix A. The same parameters for C and γ_T^* are applied to all basins. We validate the results by the following sieve criteria, summarized in Fig. 4:

Criterion (1): Freezing must not occur in the first box B_1 of any basin, *i.e.*, the ocean box closest to the grounding line. Freezing in box B_1 would increase ambient salinity, and since the overturning circulation in ice-shelf cavities is mainly haline-driven, the circulation would shut down, violating the model assumption $q > 0$ (see Sect. 2). As shown in the upper left panel of Fig. 4, the condition is not met for a combination of relatively high turbulent heat exchange and relatively low overturning
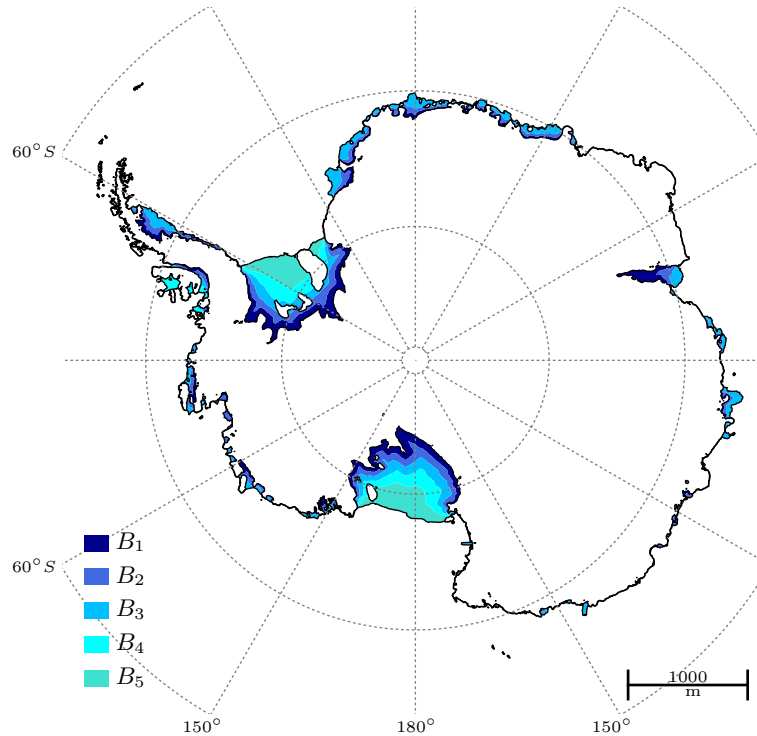
Figure 3. Extent of PICO ocean boxes for Antarctic ice shelves. Most ice shelves are split into two, three or four ocean boxes interacting with the ice cells on a much higher resolution. The largest ice shelves, Filchner-Ronne and Ross, have five ocean boxes. One ocean box typically corresponds to many ice shelf grid cells.

parameters. In such cases, freezing near the grounding line occurs because of the strong heat exchange between the ambient ocean and the ice-ocean boundary in box B_1 that cannot be balanced by the resupply of heat from the open ocean through overturning.

Criterion (2): Sub-shelf melt rates must decrease between the first and second box for each basin. This condition is based on general observations of melt-rate patterns and on the assumption that ocean water masses move consecutively through the boxes and cool down along the way, as long as melting in these boxes outweighs freezing. As shown in the lower left panel in Fig. 4, this condition is violated for either high overturning and low turbulent heat exchange or, vice versa, low overturning and high turbulent heat exchange. An appropriate balance between the strength of these values is hence necessary for a realistic melt rate pattern.

If criterion (1) or (2) fails, basic assumptions of PICO are violated. Thus, we choose the model parameters γ_T^* and C such that both criteria are strictly met. The following quantitative criteria (3) and (4) compare modeled average melt rates with observations and thus depend on our choice of valid ranges. We choose basin 1 and 14 to further constrain our model parameters for Antarctica. Basin 1 contains the Filchner-Ronne Ice Shelf and basin 14 the ice shelves in the Amundsen Sea. These two basins represent two different types of ice shelves regarding both the mode of melting and the ice-shelf size.
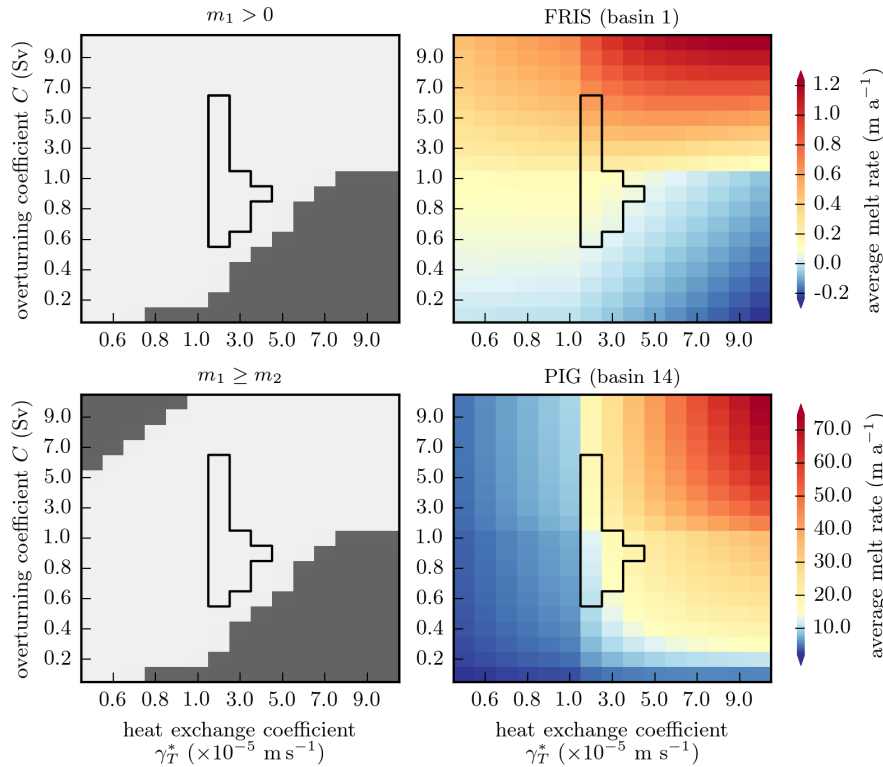
Figure 4. Sensitivity of PICO sub-shelf melt rates to the overturning coefficient C and the effective turbulent heat exchange coefficient γ_T^*.
Black contour indicates the valid range of parameters, all other parameter combinations are excluded by one of the following criteria: (Upper
left) No freezing may occur in the first ocean box, (Lower left) mean basal melt rates must decrease between the first and second ocean box,
(Upper right) mean basal melt rates for Filchner-Ronne Ice Shelf should be within the range of 0.05 to $1.0\,\mathrm{m\,a^{-1}}$, (Lower right) mean basal
melt rates for the basin containing Pine Island Glacier should be within the range of 10 to $20\,\mathrm{m\,a^{-1}}$.

Criterion (3): Average melt rates in Filchner-Ronne Ice Shelf comply with the classification of a "cold" cavity and lie
between 0.05 and $1.0\,\mathrm{m\,a^{-1}}$ (Fig. 4, upper right panel).

Criterion (4): In the Amundsen basin, for "warm" ocean conditions, average melt rates lie between 10 and $20\,\mathrm{m\,a^{-1}}$ (Fig. 4,
lower right panel).

5   Generally, an increase in overturning strength C will supply more heat and thus yield higher melt rates, especially for the
large and "cold" ice shelves like Filchner-Ronne. In the valid parameter range, larger C leads to higher melt rates also in the
smaller and "warm" basins like Pine-Island but the effect is less pronounced. In contrast, the turbulent heat exchange alters
melting particularly in basins with small ice shelves while it might decrease melt rates in large ice shelves with "cold" cavities.
Hence, modeled melting in the Filchner-Ronne basin is dominated by overturning while in the Amundsen region melting is

11

dominated by turbulent exchange across the ice-ocean boundary layer. For three different parameter combinations, the resulting spatial patterns of melt rates in the Filchner-Ronne and Pine Island regions are displayed in Fig. S.1.

All of the above criteria restrict the parameter space to a bounded set with lower and upper limits as depicted by the contour line in Fig. 4. The valid range of model parameters with C around $1\,\mathrm{Sv}$ and γ_T^* around $2 \times 10^{-5}\,\mathrm{m\,a^{-1}}$ compares well with those found in OH10 and Holland and Jenkins (1999).

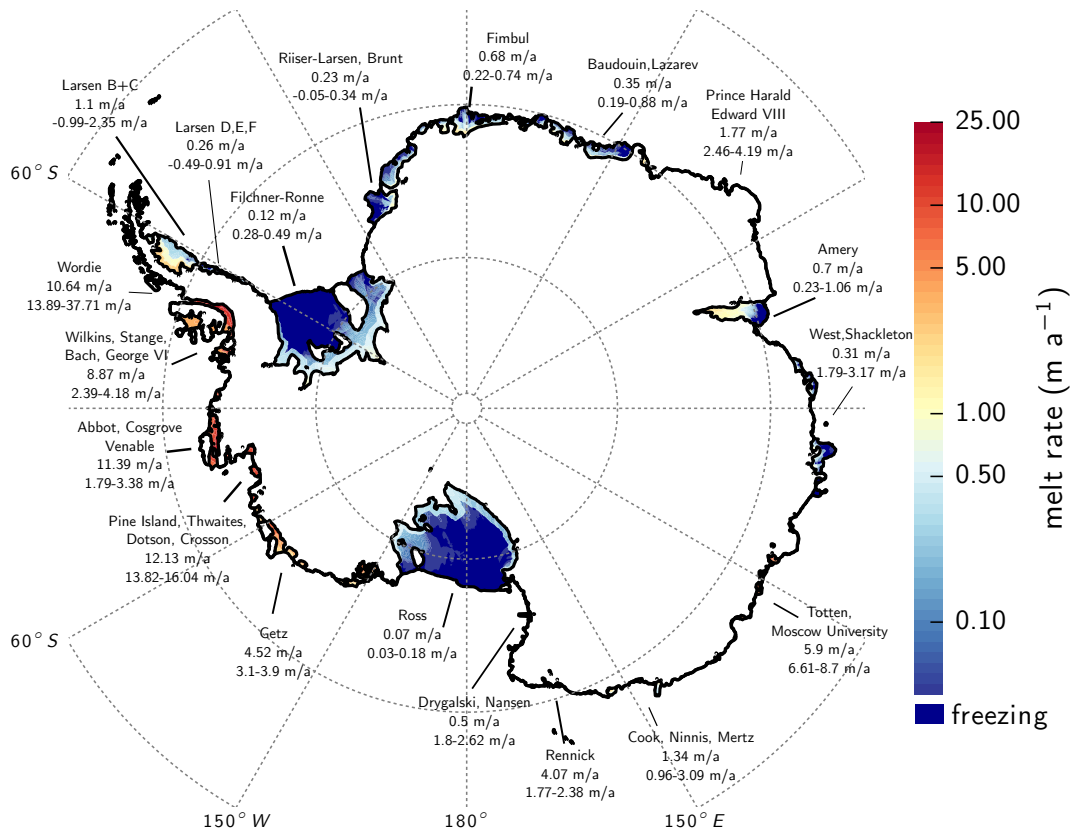## 3.2 Diagnostic melt rates for present-day Antarctica

Figure 5. Sub-shelf melt rates for present-day Antarctica computed with PISM+PICO. For each basin, the mean melt rate (upper numbers) is compared to the observed range (lower numbers) from Rignot et al. (2013). In the model, the same parameters $\gamma_T^* = 2 \times 10^{-5}\,\mathrm{m\,s^{-1}}$ and $C = 1\,\mathrm{Sv}$ are applied to all ice shelves around Antarctica. The respective oceanic boundary condition are shown in Fig. 2. Ice geometry and bedrock topography are from the BEDMAP2 data set on $5\mathrm{km}$ resolution (Fretwell et al., 2013). Refreezing occurs in some parts of the larger shelves like Filchner-Ronne and Ross.

Using the best-fit values $C = 1\,\mathrm{Sv}$ and $\gamma_T^* = 2 \times 10^{-5}\,\mathrm{m\,s^{-1}}$ found in Sect. 3.1, we apply PICO to present-day Antarctica, solving for sub-shelf melt rates and water properties in the ocean boxes. This model simulation is referred to as "reference simulation" hereafter.
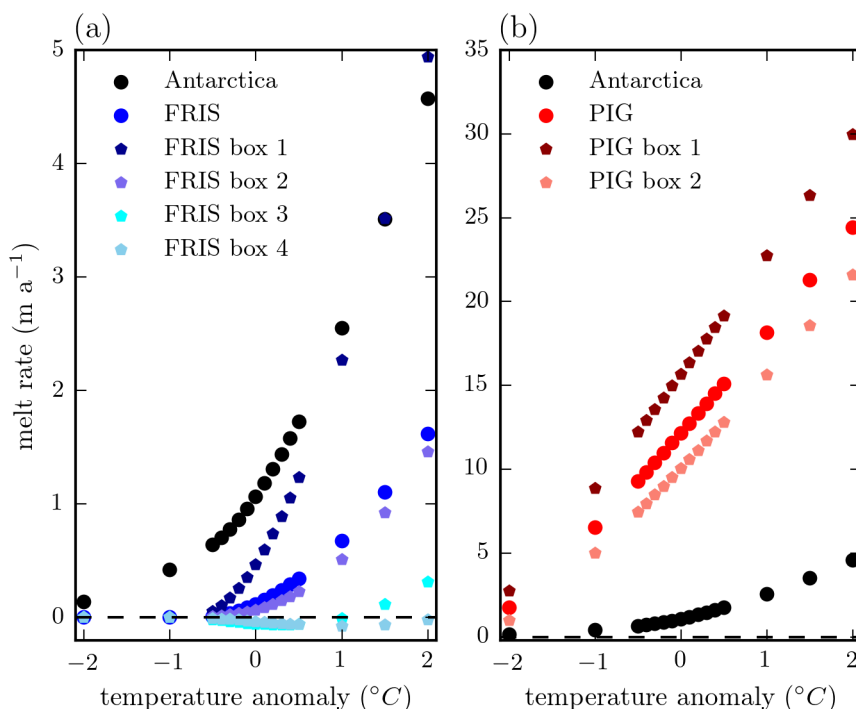
Figure 6. Sensitivity of PICO sub-shelf melt rates to ocean temperature changes for entire Antarctica (black), Filchner-Ronne Ice Shelf (blue) and the basin containing Pine Island Glacier (red). Ocean input temperatures are varied by $0.1°$C up to $2°$C. Melting depends quadratically on temperature for "cold" cavities like the one adjacent to Filchner-Ronne, and linearly for "warm" cavities like the ones in the Amundsen Region.

The average melt rates computed with PICO range from $0.07 \, \mathrm{m \, a^{-1}}$ under the Ross Ice Shelf to $12.13 \, \mathrm{m \, a^{-1}}$ for the Amundsen Region (Fig. 5). Generally, melt rates are highest in the vicinity of the grounding line and decrease towards the calving front. In some regions of the large ice shelves, refreezing occurs, *e.g.*, towards the center of Filchner-Ronne or Amery ice shelves. The melt pattern also depends on the local pressure melting temperature, which is a function of the local ice thickness.

5 Thus, in some boxes freezing occurs in regions of relatively thin ice while melting occurs in regions where the ice shelf is thicker. For the vast majority of ice shelves, the modeled average melt rates compare well with the observed ranges derived from Table 1 in Rignot et al. (2013). An exception are the two basins containing Abbot and Cosgrove ice shelves (basin 15) as well as Wilkins and Stange ice shelves (basin 16) with average modeled melt rates of $11.39 \, \mathrm{m \, s^{-1}}$ and $8.87 \, \mathrm{m \, s^{-1}}$ respectively, which is much higher than the observed range of $1.8 - 3.4 \, \mathrm{m \, s^{-1}}$ and $2.39 - 4.18 \, \mathrm{m \, s^{-1}}$. This is most likely due to the ocean

10 temperature input for these basins ($1.04 \, °$C and $1.16 \, °$C, see Fig. 2) which is higher than for the basin containing Pine Island located nearby ($0.47°$C, basin 14), explaining why the melt rates are of the same order of magnitude in these basins. Modifica-

Table 2. Results from the reference simulation as displayed in Fig. 5.

	basin	b_n	T_0	S_0	T_n	S_n	ΔT	ΔS	q	m	$m_{observed}$
Filchner-Ronne	1	5	-1.76	34.65	-2.13	34.48	-0.37	-0.17	0.19	0.12	0.28-0.49
Riiser-Larsen, Brunt	2	3	-1.66	34.53	-2.02	34.36	-0.36	-0.17	0.09	0.23	-0.05-0.34
Fimbul	3	3	-1.58	34.32	-2.03	34.12	-0.45	-0.21	0.10	0.68	0.22-0.74
Lazarev, Baudouin	4	3	-1.55	34.33	-2.01	34.11	-0.47	-0.22	0.12	0.35	0.19-0.88
Prince Harald, Edward VIII	5	3	-1.51	34.33	-1.90	34.15	-0.38	-0.18	0.08	1.77	2.46-4.19
Amery	6	3	-1.72	34.53	-2.08	34.37	-0.35	-0.16	0.12	0.70	0.23-1.06
West, Shackleton	7	3	-1.69	34.48	-2.00	34.34	-0.31	-0.14	0.09	0.31	1.79-3.17
Totten, Moscow University	8	2	-0.68	34.57	-1.56	34.16	-0.88	-0.41	0.20	5.90	6.61-8.70
Cook, Ninnis, Mertz	9	3	-1.62	34.58	-2.04	34.38	-0.43	-0.20	0.09	1.34	0.96-3.09
Rennick	10	2	-1.31	34.67	-1.69	34.49	-0.38	-0.18	0.08	4.07	1.77-2.38
Drygalski, Nansen	11	3	-1.84	34.78	-2.00	34.71	-0.16	-0.08	0.03	0.50	1.80-2.62
Ross	12	5	-1.58	34.63	-2.05	34.40	-0.47	-0.22	0.17	0.07	0.03-0.18
Getz	13	3	-0.37	34.41	-1.81	33.75	-1.44	-0.66	0.31	4.52	3.10-3.90
PIG, Thwaites, Dotson, Crosson	14	2	0.46	34.55	-0.90	33.93	-1.35	-0.62	0.23	12.13	13.82-16.04
Abbot, Cosgrove, Venable	15	3	1.04	34.69	-1.15	33.68	-2.19	-1.01	0.35	11.39	1.79-3.38
Wilkins, Stange, Bach, George VI	16	4	1.17	34.67	-1.46	33.45	-2.64	-1.21	0.35	8.87	2.39-4.18
Wordie	17	2	0.23	34.53	-0.03	34.41	-0.26	-0.12	0.06	10.64	13.89-37.71
Larsen B,C	18	3	-1.23	34.58	-1.99	34.23	-0.76	-0.35	0.17	1.10	-0.99-2.35
Larsen D,E,F	19	2	-1.79	34.66	-1.93	34.60	-0.14	-0.06	0.04	0.26	-0.49-0.91

Basins are labeled according to prominent ice shelves; b_n is the number of boxes, T_0 (S_0) is the temperature (salinity) in ocean box B_0, T_n (S_n) the temperature (salinity) averaged over the ocean box at the ice shelf front, $\Delta T = T_n - T_0$ and $\Delta S = S_n - S_0$. m is the average sub-shelf melt rate, $m_{observed}$ the uncertainty range of observed melt rates calculated from Rignot et al. (2013). q is the overturning flux. Unit of temperatures is $^\circ$C, salinity is given in PSU, melt rates in $\mathrm{m\,a^{-1}}$ and overturning flux in Sv.

tion of water masses flowing into the shelf cavities, not captured by PICO, might explain the low observed melt rates in basins 15 and 16 despite the relatively high ocean temperatures.

For all basins, ocean temperatures and salinities consistently decrease in overturning direction, *i.e.,* from the ocean reservoir box B_0 to the last box adjacent to the ice front B_n, as shown in Table 2. Most basins contain small areas in which ocean water freezes to the ice shelf base, with a maximum rate of $-0.63\,\mathrm{m\,s^{-1}}$ for the Amery Ice Shelf, see Table S.1. No freezing occurs at the Western Antarctic Peninsula nor in the Amundsen and Bellingshausen Seas. A detailed map of sub-shelf melt rates in this region as well as for Filchner-Ronne Ice Shelf can be found in Fig. S.1. For the Filchner-Ronne Ice Shelf melt rates vary between $-0.49\,\mathrm{m\,a^{-1}}$ and $1.76\ \mathrm{m\,a^{-1}}$ and for the basin containing Pine Island Glacier, melt rates range from $8.87\,\mathrm{m\,a^{-1}}$ to $18.85\,\mathrm{m\,a^{-1}}$.

Aggregated over all Antarctic ice shelves, the total melt flux is $1,299\,\mathrm{Gt\,a^{-1}}$, close to the observed estimate of $1,500\pm237$ $\mathrm{Gt\,a^{-1}}$ (Rignot et al., 2013). Overturning fluxes in our reference simulation range from 0.03 Sv for the basin containing the

small ice shelves Drygalski and Nansen to 0.35 Sv along the Western Antarctic Peninsula. These overturning fluxes compare well with the estimates in OH10.

PICO solves the system of governing equations locally in each ice-model grid cell and calculates input for each ocean box as an average along the boxes boundary as described in Sect. 2.4. Due to this model assumptions, mass and energy are a-priori not

5 perfectly conserved. In Table S.1, we compare (within each basin) heat fluxes into the ice shelf cavities with the heat flux out of the cavities into the ocean and the latent heat flux for melting. For the whole of Antarctica, the deviation in heat flux is -282.15 $\mathrm{GJ\,s^{-1}}$ which is equivalent to 2.0% of the latent heat flux for melting. The per-basin deviations are generally low ($< 15\%$), except around Amery and Filchner-Ronne ice shelves. This can be explained by an underestimation of the overturning in these particular basins, which is due to the computation of the overturning flux q along the boundary between boxes B_1 and B_2 (at a

10 depth of $423\,\mathrm{m}$ and $700\,\mathrm{m}$, respectively) instead of using the average shelf depth in B_1 (which is $671\,\mathrm{m}$ and $839\,\mathrm{m}$). Summed over all Antarctic ice shelves, the error in overturning introduced by this choice of implementation is however small. In PICO we assume q to be constant, neglecting changes due to melt water input along the shelf base. This melt water input amounts to 3.17% or less of the overturning flux within each basin, and 1.4% for the entire continent, discussed in Sect. 2.1.

Melt rates are strongly affected by changes in the ambient ocean temperatures, see Fig. 6. The dependence is approximately

15 linear for high and quadratic for lower ambient ocean temperatures. This relationship is similar to the one observed in OH10 and as expected from the governing equations. In Pine Island Glacier, melt rates increase by approximately $6\,\mathrm{m\,a^{-1}}$ per degree of warming. Changes in the ice-sheet model resolution have little effect on the resulting melt rates (Fig. S.2). For increasing the maximum number of boxes n_{max}, average melt rates converge to almost constant values for $n_{\mathrm{max}} \geq 5$ within all basins, compare Fig. S.3.

20 4 Discussion

PICO models the dominant vertical overturning circulation in ice shelf cavities and translates ocean conditions in front of the ice shelves, either from observations or large-scale ocean models, into physically-based sub-shelf melt rates. For present-day ocean fields and ice-shelf cavity geometries, PICO as an ocean module in PISM reproduces average melt rates of the same order of magnitude as observations for all Antarctic basins. With a single combination of overturning parameter C and

25 effective turbulent heat exchange parameter γ_T^* applied to all basins, a wide range of melt rates for the different ice shelves is obtained, reproducing the large-scale patterns observed in Antarctica. The results are consistent across different ice-sheet and cavity model resolutions. Additionally, PICO reproduces the common pattern of maximum melt close to the grounding line and decreasing melt rates towards the ice shelf front, eventually with re-freezing in the shallow parts of the large ice shelves. The governing model equations are solved for individual grid cells of the ice sheet model (and not for each ocean box with

30 representative depth value), which yields a comparably high resolution of the obtained melt rate field.

In the underlying equations, transversal transport within the ice shelf cavities, *e.g.*, due to Coriolis force is not represented. Seasonal melt rate variation due to intrusion of warm water from the calving front during Austral summer is also not included in the model. Boundary conditions as input for the next-following ocean box are evaluated as mean along the inter-box boundary,

which permits a smooth distribution of modeled melt rates across the ice shelves. For the entire continent, the relative error in the overturning flux introduced by averaging along the boundary as compared to the mean over the entire ocean box is 3.5%. For the estimated heat fluxes, the relative error is lower than 2.0% of the latent heat flux due to sub-shelf melting. Regarding mass conservation the relative error introduced by assuming the overturning to be constant along the boxes is below 1.4% of

5 the total overturning strength. We hence consider our choice of model simplifications as justified regarding the associated small errors introduced in the heat and mass balances for our reference simulation.

In PICO, melt rates show a quadratic dependency on ocean temperature input for lower temperatures, *e.g.*, in the Filchner-Ronne basins, and a rather linear dependency for higher temperatures, *e.g.*, in the Amundsen basin. This is consistent with the results from OH10 and the implemented melting physics assuming a constant coefficient for turbulent heat exchange.

10 In contrast, Holland et al. (2008b) employ a dependency of the turbulent heat exchange coefficient on the velocity of the overturning circulation, suggesting melt rates to respond quadratically to warming of the ambient ocean water. Here we follow the approach taken in OH10.

PICO is computationally very fast, as it uses analytic solutions of the equations of motion with a small number of boxes along the ice shelf. As boundary conditions for PICO are aggregated based on predefined regional basins, the model can act as

15 an efficient coupler of large-scale ice-sheet and ocean models. For this purpose, heat flux into the ice should be added to the boundary layer melt formulation.

5 Conclusions

The Antarctic Ice Sheet plays a vital role in modulating global sea level. The ice grounded below sea level in its marine basins is susceptible to ocean forcing and responds nonlinearly to changes in ocean boundary conditions (Mercer, 1978; Schoof, 2007).

20 We therefore need carefully estimated conditions at the ice-ocean boundary to better constrain the dynamics of the Antarctic ice and its contribution to sea-level rise for the past and the future.

The PICO model presented here provides a physics-based yet efficient approach for estimating the ocean circulation below ice shelves and the heat provided for ice shelf melt. The model extends the one-horizontal-dimensional ocean box model by OH10 to realistic ice shelf geometries following the shape of the grounding line and calving front. PICO is a comparably

25 simple and fast alternative to full ocean models, but goes beyond local melt parameterizations, which do not fully reflect the circulation below ice shelves. We validated the model using present-day ocean conditions and ice geometries. PICO accurately reproduces the general pattern of ice shelf melt, with high melting at the grounding line and low melting or refreezing towards the calving front. Its sensitivity to changes in input ocean temperatures and model parameters is comparable to earlier estimates (Holland and Jenkins, 1999; Olbers and Hellmer, 2010). The model accurately captures the large variety of observed Antarctic

30 melt rates using only two calibrated parameters that are valid for the whole ice sheet.

The ocean models that are part of the large Earth system and global circulation models do not yet resolve the circulation below ice shelves. PICO is able to fill this gap and can be used as an intermediary between global circulation models and ice sheet models. We expect that PICO will be useful for providing ocean forcing to ice sheet models with the standardized input

from climate model intercomparison projects like CMIP5 and CMIP6 (Taylor et al., 2012; Meehl et al., 2014; Eyring et al., 2016). Since PICO can deal with evolving ice shelf geometries in a computationally efficient way, it is in particular suitable for modeling the ice sheet evolution on paleo-climate timescales as well as for future projections.

PICO is implemented as a module in the open-source Parallel Ice Sheet Model (PISM). The source code is fully accessible
5 and documented as we want to encourage improvements and implementation in other ice sheet models. This includes the adaption to other ice sheets than present-day Antarctica.

6 Code availability

The PICO code is part of the PISM-PIK development branch and openly available[4]. A merge into the general PISM stable version 08 is underway.

10 Appendix A: Derivation of the analytic solutions

Here, we derive the analytic solutions of the equations system describing the overturning circulation (see Sect. 2.1) and the melting at the ice-ocean interface (see Sect. 2.2).

For box B_k with $k > 1$ we solve progressively for melt rate m_k, temperature T_k and salinity S_k in box B_k, dependent on the local pressure p_k, the area of box adjacent to the ice shelf base A_k and the temperature T_{k-1} and salinity S_{k-1} of the upstream
15 box B_{k-1}. For box B_1, we additionally solve for the overturning q as explained below. These derivations advance the ideas presented in the appendix of OH10. Assuming steady state conditions, the balance equations Eqs. 1 and 2 for box B_k from Sect. 2.1 are

$$0 = q(T_{k-1} - T_k) + A_k \gamma_T (T_{bk} - T_k) + A_k m_k (T_{bk} - T_k)$$
$$0 = q(S_{k-1} - S_k) + A_k \gamma_S (S_{bk} - S_k) + A_k m_k (S_{bk} - S_k) \tag{A1}$$

20 The heat fluxes balance at the boundary layer interface, $i.e.$, the heat flux across the boundary layer due to turbulent mixing $Q_T = \rho_w c_p \gamma_T (T_{bk} - T_k)$ equals the heat flux due to melting or freezing $Q_{Tb} = -\rho_i L m_k$, omitting the heat flux into the ice. This yields

$$\gamma_T (T_{bk} - T_k) = -\nu \lambda m_k, \tag{A2}$$

where $\nu = \rho_i / \rho_w \sim 0.89$, $\lambda = L/c_p \sim 84°C$. Regarding the salt flux balance in the boundary layer, with $Q_S = \rho_w \gamma_S (S_{bk} - S_k)$
25 at the lower interface of the boundary layer and "virtual" salt flux due to meltwater input $Q_{Sb} = -\rho_i S_{bk} m_k$, we obtain

$$\gamma_S (S_{bk} - S_k) = -\nu S_{bk} m_k. \tag{A3}$$

---

[4]https://github.com/pism/pism

Inserting Eqs. A2 and A3 into Eqs. A1 yields

$$0 = q(T_{k-1} - T_k) - A_k m_k \nu \lambda + A_k m_k (T_{bk} - T_k)$$

$$0 = q(S_{k-1} - S_k) - A_k m_k \nu S_{bk} + A_k m_k (S_{bk} - S_k).$$

Comparing $(T_{bk} - T_K) << \nu \lambda \approx 75\,°C$, allows us to neglect the last term in the temperature equation. Considering the last
two terms of the salinity equation, we find that $S_k > (1 - \nu)S_{bk} \approx 0.1\,S_{bk}$, allowing us to neglect the terms containing S_{bk},
which simplifies the equations to

$$0 = q(T_{k-1} - T_k) - A_k \nu \lambda m_k$$

$$0 = q(S_{k-1} - S_k) - A_k m_k S_k. \tag{A4}$$

We use a simplified version of the melt law described by McPhee (1992) and detailed in Sect. 2.2, which makes use of Eqn. 6
and Eqn. 5 in which the salinity in the boundary layer S_{bk} is replaced by salinity of the ambient ocean water.

$$m_1 = -\frac{\gamma_T^*}{\nu \lambda}(aS_k + b - cp_k - T_k). \tag{A5}$$

Holland and Jenkins (1999) suggest that this simplification requires γ_T^* to be a factor of 1.35 to 1.6 smaller than γ_T in the
3-equation formulation for the constant values of γ_T ranging from 3×10^{-5} m s^{-1} to 5×10^{-5} m s^{-1} used in OH10. This
implies that γ_T^* ranges from 2.2×10^{-5} m s^{-1} to 3.2×10^{-5} m s^{-1}, which is consistent with the parameter range we derive in
Sect. 3.1. Inserting the simplified melt law in Eqs. A4 yields

$$0 = q(T_{k-1} - T_k) + A_k \frac{\gamma_T^*}{\nu \lambda}(aS_k + b - cp_k - T_k)\,\nu \lambda$$

$$0 = q(S_{k-1} - S_k) + A_k \frac{\gamma_T^*}{\nu \lambda}(aS_k + b - cp_k - T_k)\,S_1$$

Replacing $x = T_{k-1} - T_k$, $y = S_{k-1} - S_k$, $T^* = aS_{k-1} + b - cp_k - T_{k-1}$, $g_1 = A_k \gamma_T^*$ and $g_2 = \frac{g_1}{\nu \lambda}$, we obtain

$$0 = qx + g_1(T^* + x - ay) \tag{A6}$$

$$0 = qy + g_2(S_{k-1} - y)(T^* + x - ay) \tag{A7}$$

We simplify the previous equations as follows. Rewriting Eq. A6

$$(T^* + x - ay) = \frac{-qx}{g_1}$$

and inserting it into Eq. A7, we obtain

$$0 = qy + g_2(S_{k-1} - y)\left(-\frac{qx}{g_1}\right) = qy - qx\frac{S_{k-1} - y}{\nu \lambda}$$

$$\Longleftrightarrow 0 = \nu \lambda y - S_{k-1}x + xy$$

$$\Longleftrightarrow 0 = (\nu \lambda + x)y - S_{k-1}x$$

$$\Rightarrow y = \frac{S_{k-1}x}{\nu \lambda + x}.$$

The Cryosphere
Discussions

Open Access

Note that we can divide the first line by q since, by the model assumptions, $q > 0$. Because $x = T_{k-1} - T_k << \nu\lambda \approx 75\,°\mathrm{C}$, we may approximate

$$y \approx \frac{S_{k-1}x}{\nu\lambda}. \tag{A8}$$

Using this approximation, we may proceed to solve the system of equations. Since we also need to solve for the overturning q in box B_1, which is adjacent to the grounding line, a slightly different approach is needed than for the other boxes, as discussed in the next section.

Solution for box B_1

The overturning flux q is parameterized as

$$q = C\rho_* \left(\,\beta(S_0 - S_1) - \alpha(T_0 - T_1)\,\right), \tag{A9}$$

in the model, see Sect. 2.1. Substituting this equation into Eqs. A6 and A7, we obtain

$$0 = \alpha x^2 - \beta xy - \frac{g_1}{C\rho_*}(T^* + x - ay) \tag{A10}$$

$$0 = -\beta y^2 + \alpha xy - \frac{g_2}{C\rho_*}(S_0 - y)(T^* + x - ay). \tag{A11}$$

Inserting the approximation for y from Eqn. A8 into the Eqn. A10, we obtain a quadratic equation for x,

$$(\beta s - \alpha)x^2 + \frac{g_1}{C\rho_*}(T^* + x(1 - as)) = 0$$

with $s = S_0/\nu\lambda$. Since $as = -0.057 \times S_0/74.76 = -0.000762 \times S_0 << 1$, we can omit the last part of the last term,

$$(\beta s - \alpha)x^2 + \frac{g_1}{C\rho_*}(T^* + x) = 0.$$

Rearranging (assuming that $\beta s - \alpha > 0$, which we demonstrate below), we obtain

$$x^2 + \frac{g_1}{C\rho_*(\beta s - \alpha)}x + \frac{g_1 T^*}{C\rho_*(\beta s - \alpha)} = 0,$$

and hence we obtain the solution

$$x = -\frac{g_1}{2C\rho_*(\beta s - \alpha)} \pm \sqrt{\left(\frac{g_1}{2C\rho_*(\beta s - \alpha)}\right)^2 - \frac{g_1 T^*}{C\rho_*(\beta s - \alpha)}}. \tag{A12}$$

The temperature in the box B_1 near the grounding line is supposed to be smaller than in the ocean box B_0, since, in general, melting will occur in box B_1 and hence $T_1 < T_0$, or equivalently $x = T_0 - T_1 > 0$. Furthermore, we know that $g_1/(C\rho_*) = A_1\gamma_T^*/(C\rho_*)$ is positive, as all factors are positive. Since $\alpha = 7.5 \times 10^{-5}$, $\beta = 7.7 \times 10^{-4}$ and $s = S_0/(\nu\lambda) = S_0/74.76 \geq 0.4$, it follows that $\beta s > \alpha$. This means that the first summand of Eqs. A12 is negative and the second (negative) solution can be excluded. From here, we use $T_1 = T_0 + x$ and $y = xS_0/(\nu\lambda)$ to solve for T_1, S_1, m_1 and q.

Solution for box B_k, $k > 1$

Now, we give the solution for the other boxes B_k with $k > 1$. By inserting the approximation for y in Eqs A8 into Eq. A6, we can solve for x as

$$0 = qx + g_1 \left(T^* + x - a \frac{S_{k-1} x}{\nu \lambda} \right)$$

$$\Longleftrightarrow 0 = qx + g_1 T^* + g_1 x - g_2 \, a \, S_{k-1} \, x$$

$$\Longleftrightarrow -g_1 T^* = x(q + g_1 - g_2 \, S_{k-1} \, a)$$

$$\Longleftrightarrow x = \frac{-g_1 T^*}{q + g_1 - g_2 \, a \, S_{k-1}}. \tag{A13}$$

The denominator is positive, as all terms are positive, and the sign of the numerator depends on T^*. The equation can now be solved for T_k, and then Eqn. A8 for S_k and Eqn. 13 for m_k.

Appendix B: Motivation for geometric rule

Here, we want to motivate the rule that determines the extent of the boxes under each ice shelf. The rule aims at equal areas for all boxes. Assuming a half-circle with radius $r = 1$, we want to split it into a fixed number n of equal-area rings. Generalized to the individual shapes of ice-shelf basins, we will define the "radius" of an ice shelf as $r = 1 - d_{\mathrm{GL}}/(d_{\mathrm{GL}} + d_{\mathrm{IF}})$. We define $r_1 = 1$ the outer (grounding-line ward) radius of the half-circle ring covering an area A_1 and corresponding to box B_1 adjacent to the grounding line, r_2 as the outer radius of second outer-most half-ring, etc. The box B_k is then given by all shelf cells with horizontal coordinates (x, y) such that $r_{k+1} \leq r(x, y) \leq r_k$ where $r_{n+1} = 0$ is the center point of the circle. We can use these to determine the areas $A_n = 0.5 \pi r_n^2$, $A_{n-1} = 0.5 \pi (r_{n-1}^2 - r_n^2)$, ..., $A_{n-k} = 0.5 \pi (r_{n-k}^2 - r_{n-k+1}^2)$. If we require that $A_1 = A_2 = \cdots = A_n$, then, solving progressively, $r_{n-k} = \sqrt{k+1}\, r_n$. By our assumption is $r_1 = 1$, hence $1 = r_{n-(n-1)} = \sqrt{n}\, r_n$. This implies that $r_n = 1/\sqrt{n}$ and thus $r_{n-k} = \sqrt{\frac{k+1}{n}}$. Hence, the box B_k for $k = 1, \ldots, n$ is defined as $1 - \sqrt{(n-k+1)/n} \leq d_{\mathrm{GL}}/(d_{\mathrm{GL}} + d_{\mathrm{IF}}) \leq 1 - \sqrt{(n-k)/n}$.

References

Asay-Davis, X. S., Cornford, S. L., Durand, G., Galton-Fenzi, B. K., Gladstone, R. M., Gudmundsson, G. H., Hattermann, T., Holland, D. M., Holland, D., Holland, P. R., Martin, D. F., Mathiot, P., Pattyn, F., and Seroussi, H.: Experimental design for three interrelated marine ice sheet and ocean model intercomparison projects: MISMIP v. 3 (MISMIP+), ISOMIP v. 2 (ISOMIP+) and MISOMIP v. 1 (MISOMIP1), Geoscientific Model Development, 9, 2471–2497, doi:10.5194/gmd-9-2471-2016, 2016.

Beckmann, A. and Goosse, H.: A parameterization of ice shelf–ocean interaction for climate models, Ocean Modelling, 5, 157 – 170, doi:http://dx.doi.org/10.1016/S1463-5003(02)00019-7, 2003.

Bueler, E. and Brown, J.: Shallow shelf approximation as a "sliding law" in a thermomechanically coupled ice sheet model, Journal of Geophysical Research, 114, doi:10.1029/2008JF001179, 2009.

Carroll, D., Sutherland, D. A., Shroyer, E. L., Nash, J. D., Catania, G. A., and Stearns, L. A.: Modeling Turbulent Subglacial Meltwater Plumes: Implications for Fjord-Scale Buoyancy-Driven Circulation, Journal of Physical Oceanography, 45, 2169–2185, doi:10.1175/JPO-D-15-0033.1, 2015.

De Rydt, J. and Gudmundsson, G. H.: Coupled ice shelf-ocean modeling and complex grounding line retreat from a seabed ridge, Journal of Geophysical Research: Earth Surface, 121, 865–880, doi:10.1002/2015JF003791, 2015JF003791, 2016.

Depoorter, M. a., Bamber, J. L., Griggs, J. a., Lenaerts, J. T. M., Ligtenberg, S. R. M., van den Broeke, M. R., and Moholdt, G.: Calving fluxes and basal melt rates of Antarctic ice shelves., Nature, 502, 89–92, doi:10.1038/nature12567, 2013.

Dupont, T. K. and Alley, R. B.: Assessment of the importance of ice-shelf buttressing to ice-sheet flow, Geophysical Research Letters, 32, doi:10.1029/2004GL022024, l04503, 2005.

Eyring, V., Bony, S., Meehl, G. A., Senior, C. A., Stevens, B., Stouffer, R. J., and Taylor, K. E.: Overview of the Coupled Model Intercomparison Project Phase 6 (CMIP6) experimental design and organization, Geoscientific Model Development, 9, 1937–1958, doi:10.5194/gmd-9-1937-2016, 2016.

Favier, L., Durand, G., Cornford, S. L., Gudmundsson, G. H., Gagliardini, O., Gillet-Chaulet, F., Zwinger, T., Payne, A. J., and Le Brocq, a. M.: Retreat of Pine Island Glacier controlled by marine ice-sheet instability, Nature Climate Change, 5, 117–121, doi:10.1038/nclimate2094, 2014.

Feldmann, J., Albrecht, T., Khroulev, C., Pattyn, F., and Levermann, A.: Resolution-dependent performance of grounding line motion in a shallow model compared with a full-Stokes model according to the MISMIP3d intercomparison, Journal of Glaciology, 60, 353–360, doi:doi:10.3189/2014JoG13J093, 2014.

Fretwell, P., Pritchard, H. D., Vaughan, D. G., Bamber, J. L., Barrand, N. E., Bell, R., Bianchi, C., Bingham, R. G., Blankenship, D. D., Casassa, G., Catania, G., Callens, D., Conway, H., Cook, A. J., Corr, H. F. J., Damaske, D., Damm, V., Ferraccioli, F., Forsberg, R., Fujita, S., Gim, Y., Gogineni, P., Griggs, J. A., Hindmarsh, R. C. A., Holmlund, P., Holt, J. W., Jacobel, R. W., Jenkins, A., Jokat, W., Jordan, T., King, E. C., Kohler, J., Krabill, W., Riger-Kusk, M., Langley, K. A., Leitchenkov, G., Leuschen, C., Luyendyk, B. P., Matsuoka, K., Mouginot, J., Nitsche, F. O., Nogi, Y., Nost, O. A., Popov, S. V., Rignot, E., Rippin, D. M., Rivera, A., Roberts, J., Ross, N., Siegert, M. J., Smith, A. M., Steinhage, D., Studinger, M., Sun, B., Tinto, B. K., Welch, B. C., Wilson, D., Young, D. A., Xiangbin, C., and Zirizzotti, A.: Bedmap2: improved ice bed, surface and thickness datasets for Antarctica, The Cryosphere, 7, 375–393, doi:10.5194/tc-7-375-2013, 2013.

Goldberg, D. N., Little, C. M., Sergienko, O. V., Gnanadesikan, A., Hallberg, R., and Oppenheimer, M.: Investigation of land ice-ocean interaction with a fully coupled ice-ocean model: 1. Model description and behavior, Journal of Geophysical Research: Earth Surface, 117, doi:10.1029/2011JF002246, f02037, 2012.

Greenbaum, J. S., Blankenship, D. D., Young, D. a., Richter, T. G., Roberts, J. L., Aitken, a. R. a., Legresy, B., Schroeder, D. M., Warner, R. C., van Ommen, T. D., and Siegert, M. J.: Ocean access to a cavity beneath Totten Glacier in East Antarctica, Nature Geoscience, 8, doi:10.1038/NGEO2388, 2015.

Gudmundsson, G. H., Krug, J., Durand, G., Favier, L., and Gagliardini, O.: The stability of grounding lines on retrograde slopes, The Cryosphere, 6, 1497–1505, doi:10.5194/tc-6-1497-2012, 2012.

Hellmer, H. and Olbers, D.: A two-dimensional model for the thermohaline circulation under an ice shelf, Antarctic Science, 1, 325–336, doi:10.1017/S0954102089000490, 1989.

Hellmer, H. H., Kauker, F., Timmermann, R., and Hattermann, T.: The fate of the southern Weddell Sea continental shelf in a warming climate, Journal of Climate, 0, doi:10.1175/JCLI-D-16-0420.1, 2017.

Holland, D. M. and Jenkins, A.: Modeling Thermodynamic Ice–Ocean Interactions at the Base of an Ice Shelf, Journal of Physical Oceanography, 29, 1787–1800, doi:10.1175/1520-0485(1999)029<1787:MTIOIA>2.0.CO;2, 1999.

Holland, D. M., Thomas, R. H., de Young, B., Ribergaard, M. H., and Lyberth, B.: Acceleration of Jakobshavn Isbrætriggered by warm subsurface ocean waters, Nature Geoscience, 1, 659–664, doi:10.1038/ngeo316, 2008a.

Holland, P. R., Feltham, D. L., and Jenkins, A.: Ice Shelf Water plume flow beneath Filchner-Ronne Ice Shelf, Antarctica, Journal of Geophysical Research: Oceans, 112, doi:10.1029/2006JC003915, c05044, 2007.

Holland, P. R., Jenkins, A., and Holland, D. M.: The Response of Ice Shelf Basal Melting to Variations in Ocean Temperature, Journal of Climate, 21, 2558–2572, doi:10.1175/2007JCLI1909.1, 2008b.

Hutter, K.: Theoretical glaciology: material science of ice and the mechanics of glaciers and ice sheets, vol. 1, Springer, 1983.

Jacobs, S., Helmer, H., Doake, C. S. M., Jenkins, A., and Frolich, R. M.: Melting of ice shelves and the mass balance of Antarctica, Journal of Glaciology, 38, 375–387, doi:doi:10.3198/1992JoG38-130-375-387, 1992.

Jacobs, S. S., Jenkins, A., Giulivi, C. F., and Dutrieux, P.: Stronger ocean circulation and increased melting under Pine Island Glacier ice shelf, Nature Geoscience, 4, 519–523, doi:10.1038/ngeo1188, 2011.

Jenkins, A.: A one-dimensional model of ice shelf-ocean interaction, Journal of Geophysical Research: Oceans, 96, 20 671–20 677, doi:10.1029/91JC01842, 1991.

Jenkins, A.: Convection-Driven Melting near the Grounding Lines of Ice Shelves and Tidewater Glaciers, Journal of Physical Oceanography, 41, 2279–2294, doi:10.1175/JPO-D-11-03.1, 2011.

Jenkins, A., Hellmer, H. H., and Holland, D. M.: The Role of Meltwater Advection in the Formulation of Conservative Boundary Conditions at an Ice–Ocean Interface, Journal of Physical Oceanography, 31, 285–296, doi:10.1175/1520-0485(2001)031<0285:TROMAI>2.0.CO;2, 2001.

Joughin, I., Alley, R. B., and Holland, D. M.: Ice-Sheet Response to Oceanic Forcing, Science, 338, 1172–1176, doi:10.1126/science.1226481, 2012.

Joughin, I., Smith, B. E., and Medley, B.: Marine Ice Sheet Collapse Potentially Under Way for the Thwaites Glacier Basin, West Antarctica, Science, 344, 735–738, doi:10.1126/science.1249055, 2014.

Lewis, E. L. and Perkin, R. G.: Ice pumps and their rates, Journal of Geophysical Research: Oceans, 91, 11 756–11 762, doi:10.1029/JC091iC10p11756, 1986.

Little, C. M., Goldberg, D., Gnanadesikan, A., and Oppenheimer, M.: On the coupled response to ice-shelf basal melting, Journal of Glaciology, 58, 203–215, doi:doi:10.3189/2012JoG11J037, 2012.

Liu, Y., Moore, J. C., Cheng, X., Gladstone, R. M., Bassis, J. N., Liu, H., Wen, J., and Hui, F.: Ocean-driven thinning enhances iceberg calving and retreat of Antarctic ice shelves, Proceedings of the National Academy of Sciences, 112, 3263–3268, doi:10.1073/pnas.1415137112, 5   2015.

MacGregor, J. A., Catania, G. A., Markowski, M. S., and Andrews, A. G.: Widespread rifting and retreat of ice-shelf margins in the eastern Amundsen Sea Embayment between 1972 and 2011, Journal of Glaciology, 58, 458–466, doi:10.3189/2012JoG11J262, 2012.

Martin, M. A., Winkelmann, R., Haseloff, M., Albrecht, T., Bueler, E., Khroulev, C., and Levermann, A.: The Potsdam Parallel Ice Sheet Model (PISM-PIK) – Part 2: Dynamic equilibrium simulation of the Antarctic ice sheet, The Cryosphere, 5, 727–740, doi:10.5194/tc-5-10   727-2011, 2011.

McDougall, T. J. and Barker, P. M.: Getting started with TEOS-10 and the Gibbs Seawater (GSW) Oceanographic Toolbox, May, SCOR/IAPSO WG1207, http://www.teos-10.org/pubs/Getting_Started.pdf, 2011.

McPhee, M. G.: Turbulent heat flux in the upper ocean under sea ice, Journal of Geophysical Research: Oceans, 97, 5365–5379, doi:10.1029/92JC00239, 1992.

15 McPhee, M. G.: Parameterization of mixing in the ocean boundary layer, Journal of Marine Systems, 21, 55 – 65, doi:http://dx.doi.org/10.1016/S0924-7963(99)00005-6, 1999.

Meehl, G. A., Moss, R., Taylor, K. E., Eyring, V., Stouffer, R. J., Bony, S., and Stevens, B.: Climate Model Intercomparisons: Preparing for the Next Phase, Eos, Transactions American Geophysical Union, 95, 77–78, doi:10.1002/2014EO090001, 2014.

Mercer, J. H.: West Antarctic ice sheet and CO 2 greenhouse effect- A threat of disaster, Nature, 271, 321–325, 1978.

20 Moholdt, G., Padman, L., and Fricker, H. A.: Basal mass budget of Ross and Filchner-Ronne ice shelves, Antarctica, derived from Lagrangian analysis of ICESat altimetry, Journal of Geophysical Research: Earth Surface, 119, 2361–2380, doi:10.1002/2014JF003171, 2014JF003171, 2014.

Morland, L. W.: Unconfined Ice-Shelf Flow, pp. 99–116, Springer Netherlands, Dordrecht, doi:10.1007/978-94-009-3745-1_6, 1987.

Mouginot, J., Rignot, E., and Scheuchl, B.: Sustained increase in ice discharge from the Amundsen Sea Embayment, West Antarctica, from 25   1973 to 2013, Geophysical Research Letters, 41, 1576–1584, doi:10.1002/2013GL059069, 2014.

Olbers, D. and Hellmer, H.: A box model of circulation and melting in ice shelf caverns, Ocean Dynamics, 60, 141–153, doi:10.1007/s10236-009-0252-z, 2010.

Paolo, F. S., Fricker, H. A., and Padman, L.: Volume loss from Antarctic ice shelves is accelerating, Science, 348, 327–332, doi:10.1126/science.aaa0940, 2015.

30 Pattyn, F., Perichon, L., Durand, G., Favier, L., Gagliardini, O., Hindmarsh, R. C., Zwinger, T., Albrecht, T., Cornford, S., Docquier, D., Fürst, J. J., Goldberg, D., Gudmundsson, G. H., Humbert, A., Hütten, M., Huybrechts, P., Jouvet, G., Kleiner, T., Larour, E., Martin, D., Morlighem, M., Payne, A. J., Pollard, D., Rückamp, M., Rybak, O., Seroussi, H., Thoma, M., and Wilkens, N.: Grounding-line migration in plan-view marine ice-sheet models: results of the ice2sea MISMIP3d intercomparison, Journal of Glaciology, 59, 410–422, doi:doi:10.3189/2013JoG12J129, 2013.

35 Payne, A. J., Holland, P. R., Shepherd, A. P., Rutt, I. C., Jenkins, A., and Joughin, I.: Numerical modeling of ocean-ice interactions under Pine Island Bay's ice shelf, Journal of Geophysical Research: Oceans, 112, doi:10.1029/2006JC003733, c10019, 2007.

Pollard, D. and DeConto, R. M.: Description of a hybrid ice sheet-shelf model, and application to Antarctica, Geoscientific Model Development, 5, 1273–1295, doi:10.5194/gmd-5-1273-2012, 2012.

Pritchard, H. D., Ligtenberg, S. R. M., Fricker, H. A., Vaughan, D. G., van den Broeke, M. R., and Padman, L.: Antarctic ice-sheet loss driven by basal melting of ice shelves, Nature, 484, 502–505, doi:10.1038/nature10968, 2012.

Rignot, E., Jacobs, S., Mouginot, J., and Scheuchl, B.: Ice-shelf melting around Antarctica., Science, 341, 266–270, doi:10.1126/science.1235798, 2013.

5 Schmidtko, S., Heywood, K. J., Thompson, A. F., and Aoki, S.: Multidecadal warming of Antarctic waters, Science, 346, 1227–1231, doi:10.1126/science.1256117, 2014.

Schoof, C.: Marine ice-sheet dynamics. Part 1. The case of rapid sliding, Journal of Fluid Mechanics, 573, 27–55, 2007.

Seroussi, H., Nakayama, Y., Larour, E., Menemenlis, D., Morlighem, M., Rignot, E., and Khazendar, A.: Continued retreat of Thwaites Glacier, West Antarctica, controlled by bed topography and ocean circulation, Geophysical Research Letters, doi:10.1002/2017GL072910, 10 2017.

Taylor, K. E., Stouffer, R. J., and Meehl, G. A.: An Overview of CMIP5 and the Experiment Design, Bulletin of the American Meteorological Society, 93, 485–498, doi:10.1175/BAMS-D-11-00094.1, 2012.

Thoma, M., Determann, J., Grosfeld, K., Goeller, S., and Hellmer, H. H.: Future sea-level rise due to projected ocean warming beneath the Filchner Ronne Ice Shelf: A coupled model study, Earth Planet. Sci. Lett., 431, 217–224, doi:10.1016/j.epsl.2015.09.013, 2015.

15 Thomas, R. H.: Ice Shelves: a Review, Journal of Glaciology, 24, 273–286, doi:doi:10.3198/1979JoG24-90-273-286, 1979.

Winkelmann, R., Martin, M. A., Haseloff, M., Albrecht, T., Bueler, E., Khroulev, C., and Levermann, A.: The Potsdam Parallel Ice Sheet Model (PISM-PIK) – Part 1: Model description, The Cryosphere, 5, 715–726, doi:10.5194/tc-5-715-2011, 2011.

Wouters, B., Martin-Espanol, A., Helm, V., Flament, T., van Wessem, J. M., Ligtenberg, S. R., van den Broeke, M. R., and Bamber, J. L.: Glacier mass loss. Dynamic thinning of glaciers on the Southern Antarctic Peninsula, Science, 348, 899–903, 20 doi:10.1126/science.aaa5727, 2015.

Zwally, H., Giovinetto, M., Beckley, M., and Saba, J.: Antarctic and Greenland Drainage Systems, 2012.